catalysts

MDPI

Article

Relations between Structure, Activity and Stability in C_3N_4 Based Photocatalysts Used for Solar Hydrogen Production

Ramesh P. Sivasankaran [1], Nils Rockstroh [1], Dirk Hollmann [1], Carsten R. Kreyenschulte [1], Giovanni Agostini [1], Henrik Lund [1], Amitava Acharjya [2], Jabor Rabeah [1], Ursula Bentrup [1], Henrik Junge [1], Arne Thomas [2] and Angelika Brückner [1,*]

[1] Leibniz Institute for Catalysis at the University of Rostock, Albert-Einstein-Str. 29a, 18059 Rostock, Germany; Ramesh.Sivasankaran@catalysis.de (R.P.S.); Nils.Rockstroh@catalysis.de (N.R.); dirk.hollmann@uni-rostock.de (D.H.); carsten.kreyenschulte@catalysis.de (C.R.K.); giovanni.agostini@catalysis.de (G.A.); henrik.lund@catalysis.de (H.L.); Jabor.rabeah@catalysis.de (J.R.); Ursula.bentrup@catalysis.de (U.B.); Henrik.Junge@catalysis.de (H.J.)

[2] Department of Chemistry, Technical University Berlin, Hardenbergstr. 40, 10623 Berlin, Germany; amitava-_acharjya5@mailbox.tu-berlin.de (A.A.); arne.thomas@tu-berlin.de (A.T.)

* Correspondence: angelika.brueckner@catalysis.de; Tel.: +49-381-1281-244

Received: 22 December 2017; Accepted: 23 January 2018; Published: 29 January 2018

Abstract: Solar hydrogen production from water could be a sustainable and environmentally friendly alternative to fossil energy carriers, yet so far photocatalysts active and stable enough for large-scale applications are not available, calling for advanced research efforts. In this work, H_2 evolution rates of up to 1968 and 5188 μmol h^{-1} g^{-1} were obtained from aqueous solutions of triethanolamine (TEOA) and oxalic acid (OA), respectively, by irradiating composites of $AgIn_5S_8$ (AIS), mesoporous C_3N_4 (CN, surface area >150 m^2/g) and ≤2 wt.% in-situ photodeposited Pt nanoparticles (NPs) with UV-vis (≥300 nm) and pure visible light (≥420 nm). Structural properties and electron transport in these materials were analyzed by XRD, STEM-HAADF, XPS, UV-vis-DRS, ATR-IR, photoluminescence and in situ-EPR spectroscopy. Initial H_2 formation rates were highest for Pt/CN, yet with TEOA this catalyst deactivated by inclusion of Pt NPs in the matrix of CN (most pronounced at $\lambda \geq 300$ nm) while it remained active with OA, since in this case Pt NPs were enriched on the outermost surface of CN. In Pt/AIS-CN catalysts, Pt NPs were preferentially deposited on the surface of the AIS phase which prevents them from inclusion in the CN phase but reduces simultaneously the initial H_2 evolution rate. This suggests that AIS hinders transport of separated electrons from the CN conduction band to Pt NPs but retains the latter accessible by protons to produce H_2.

Keywords: $AgIn_5S_8$; C_3N_4; photocatalytic hydrogen production; TEM; XPS; in situ-EPR

1. Introduction

In light of the foreseeable depletion of fossil energy carriers, much research work has been done in recent years to explore alternative, sustainable and environmentally friendly ways of supplying energy [1,2]. Hydrogen production by photocatalytic water splitting using sunlight is one of these approaches. Since solar radiation contains visible light as the major fraction besides a small percentage of UV light only, catalysts designed for large scale application must work efficiently under irradiation with wavelengths above 400 nm [3]. Unfortunately, most of the common semiconductor-based photocatalysts, first and foremost TiO_2, but also titanates and tantalates such as $SrTiO_3$ and $NaTaO_3$, can only harvest UV light due to their large band gaps, while others have unsuitable band positions (e.g., WO_3) or are not stable (e.g., CdS) [4].

Polymeric carbon nitride, C_3N_4, is an abundant, easy-to-prepare organic semiconductor which absorbs light in the visible range. Wang et al. showed for the first time in 2009 that this material can liberate hydrogen from water using light with $\lambda > 420$ nm in the presence of methanol or triethanolamine (TEOA) as sacrificial agents [5]. Since that time, many papers on the use of differently prepared and modified C_3N_4 photocatalysts for light-driven water splitting have been published. A representative though not complete overview is given in Table S1. Among this variety of materials, those with a well-ordered graphite-like structure (g-C_3N_4) showed rather low hydrogen evolution rates, mainly due to their low surface area, low electrical conductivity, limited light absorption in the visible region and high recombination rate of charge carriers [6,7]. Therefore, various efforts have been undertaken to improve the photocatalytic activity of g-C_3N_4, e.g., by band gap engineering, morphology control, introduction of porosity and/or metal co-catalysts as well as composite formation with other compounds such as carbon nanotubes, graphene, conducting polymers, metal organic frameworks, and other semiconductors [8–10]. Among these modification strategies, developing nanocomposites of g-C_3N_4 with other semiconductors appeared to be promising since this creates synergistic heterojunctions, eventually resulting in an improved charge separation and hence high photocatalytic efficiency [11–13]. Due to the different reaction conditions (e.g., light source, co-catalysts, sacrificial agents, pH of the solution etc.), it is impossible to compare the catalytic performance of the catalysts in Table S1 directly. Yet from entries 1 and 2 of the same reference, it is evident that mesoporous C_3N_4 materials with high surface area lead to much higher H_2 evolution rates than g-C_3N_4. Therefore, we used mesoporous C_3N_4 (CN) prepared after the same protocol [14] in this work, too.

So far, two major goals for activity enhancement have been pursued by modifying C_3N_4: (1) optimization of band gap and band positions to maximize light absorption in the solar range and (2) suppression of fast recombination of separated electrons and holes in the conduction and valence band of CN. However, for application-oriented large-scale H_2 production, the long-term stability of the CN photocatalysts is at least equally important as high activity. Surprisingly, this aspect has been widely ignored so far. In most of the studies, catalytic tests have been performed only for a few hours (Table S1) and/or the catalysts were tested exclusively with visible light above ≈420 nm by using cut-off filters [5], which neglects the small percentage of UV radiation present in sunlight. Moreover, metal co-catalysts (mainly Pt) have been used in most of the CN-based photocatalytic water splitting systems (Table S1). Frequently, the co-catalyst metal particles have been formed in situ in the early stage of the reaction, by irradiating the CN photocatalyst in the presence of a solved metal precursor, e.g., H_2PtCl_6 or $Cu(NO_3)_2$ in the case of Pt [5] or Cu [15] co-catalysts, respectively. The formation process and, thus, the structure of such co-catalyst particles might strongly depend on particular properties of the reaction mixture such as the pH value which itself is governed by the nature of the sacrificial agent (SA). Systematic investigations of such effects are rare so far.

In this work, we analyzed the behaviour of photocatalysts based on composites of $AgIn_5S_8$ (AIS) with mesoporous CN in the presence of a Pt co-catalyst during photocatalytic H_2 evolution from water/SA mixtures depending on the radiation wavelength and on the pH of the reaction solution. AIS has been chosen as co-component since, as a single phase with a direct bandgap of 1.70–1.80 eV, it revealed significant H_2 evolution under visible light, though with Na_2S/Na_2SO_3 as SA [16–18] which is less useful as sacrificial agent since its oxidation produces sulfate as a byproduct (Table S2). Structure-reactivity relationships have been derived based on comprehensive catalyst characterization including in situ-electron paramagnetic resonance (EPR) spectroscopy for monitoring pathways of electron transfer. The role of the SA and AIS with respect to activity, stability and nature of the formed Pt co-catalyst is discussed.

2. Results and Discussion

2.1. Catalytic Activity

Figure 1 shows H_2 evolution as a function of time for monophasic AIS and CN as well as for AIS-CN composites with different contents of AIS under (a) UV-vis and (b) visible light irradiation ($\lambda > 420$ nm) in the presence of triethanolamine (TEOA) as sacrificial agent. Pt nanoparticles (NPs) were deposited as co-catalyst on the surface of these materials by in-situ photoreduction of H_2PtCl_6. It appeared that the total Pt content determined by ICP-OES in Pt/CN is much lower than the theoretical value of 2 wt.%, after both 3 h and 20 h irradiation with UV-vis light (0.27 and 0.43 wt.%, respectively, Table 1) while it is only slightly lower for the respective Pt/10AIS-CN samples (1.86 and 1.87 wt.%). This is probably due to the fact that not the whole amount of the solved $[PtCl_6]^{2-}$ precursor but only a part of it is reduced and deposited as Pt NPs in basic TEOA solution. It has been shown that at high pH (as in the presence of TEOA) a stepwise hydrolysis occurs according to $[PtCl_6]^{2-} \rightarrow [Pt(OH)_xCl_{6-x}]^{2-} \rightarrow [Pt(OH)_6]^{2-}$ which hampers the formation of metallic Pt particles [19]. Moreover, the rather non-polar surface of CN might be less prone than the polar AIS surface to adsorb the polar Pt complex species. Nevertheless, the small percentage of deposited Pt is obviously sufficient to account for the highest initial H_2 evolution rate of Pt/CN under UV-vis light during the first 4 h. Unfortunately, Pt/CN deactivates quickly afterwards. In contrast, deposition of 5–15% of AIS on CN reduces the initial H_2 evolution rates but retards deactivation. With 5 wt.% AIS, deactivation could be partly slowed down while 20 wt.% of AIS led to a significant activity decline over the whole range of time. A percentage of 10 wt.% AIS appeared to be the optimum. Though the initial H_2 evolution rate for this sample is markedly lower than for Pt/CN, despite a much higher total Pt content (vide infra), Pt/10AIS-CN shows negligible deactivation within 24 h. Interestingly, samples Pt/AIS without CN as well as blank CN without Pt were not active at all (Figure 1a). When a physical mixture of AIS (10 wt.%) and CN was used instead of the 10AIS-CN composite, the shape of the H_2 evolution curve showed a very similar deactivation behavior like monophasic Pt/CN (Figure 1a). When a 420 nm cut-off filter was used, H_2 production rates were lower for all samples. However, deactivation within 24 h did not occur for Pt/xAIS-CN and was much slower for Pt/CN, though it could not be completely suppressed in the latter case. This shows clearly that the stability of Pt/CN is limited in the long term even under visible light—an issue which has been widely ignored in the past.

Table 1. Surface composition derived by XPS.

Sample	Surface Content (at.%)							Total Pt (wt.%) (ICP-OES)
	C	N	O	Ag	In	S	Pt	
CN	44.8	52.3	2.9	-	-	-	-	-
AIS	22.3		9.7	4.7	27.5	35.9	-	-
10AIS-CN	42.8	34.5	7.0	1.2	6.1	8.3	-	-
Pt/CN (3 h)	45.5	50.9	3.5	-	-	-	0.06	0.27
Pt/CN (20 h)	46.6	49.4	3.9	-	-	-	0.05	0.43
Pt/CN_OA (4 h) [1]	46.9	48.5	3.7	-	-	-	0.85	1.69
Pt/CN_OA_TEOA (24 h) [2]	44.8	51.3	3.6	-	-	-	0.2	n. d.
Pt/10AIS-CN (3 h)	47.9	35.9	6.6	0.6	2.4	4.1	2.5	1.86
Pt/10AIS-CN (20 h)	45.3	40.6	7.2	0.5	2.6	2.4	1.4	1.87

[1] SA = oxalic acid, [2] Pt/CN_OA (4 h) recovered and exposed to UV-vis light for 24 h with TEOA as SA.

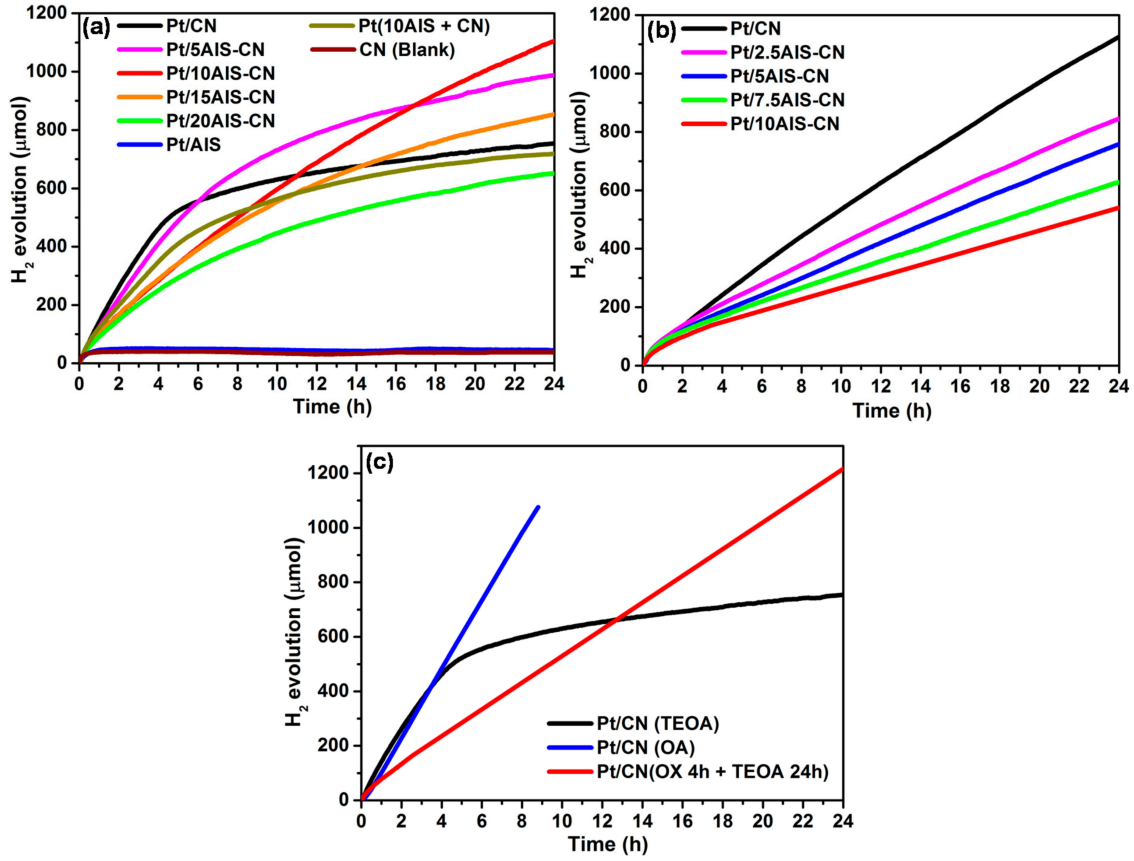

Figure 1. H_2 evolution as a function of time for monophasic CN and AIS as well as for xAIS-CN composites with x wt.% of AIS under UV-vis (**a**) and visible irradiation with $\lambda > 420$ nm (**b**); (**c**) Comparison of Pt/CN under UV-vis light with TEOA, with OA and with TEOA again after removal from OA-containing reaction mixture after 4 h. CN: mesoporous C_3N_4; AIS: $AgIn_5S_8$; TEOA: triethanolamine.

To find out whether the pH of the reaction solution, which is basic in the presence of TEOA (pH = 10.6), has an impact on the stability of the photocatalysts, an analogous experiment with Pt/CN and oxalic acid (OA) as sacrificial agent was performed at pH = 0.67 (blue line, Figure 1c). In this case, total H_2 production is much higher. This was expected, due to the higher proton concentration. It must also be mentioned, that H_2 is not only liberated from water but also from OA, since CO_2 is formed as well. However, the total Pt content as well as the surface Pt percentage of the Pt/CN catalyst are much higher in OA than in TEOA, which might lead to higher activity (Table 1). This is most probably due to the fact that direct reduction of $[PtCl_6]^{2-}$ to metallic Pt is facilitated at low pH; intermediate hydrolysis of the Pt precursor complex, as in basic medium, is avoided [19]. No deactivation of the Pt/CN catalyst occurs in the presence of OA. After 4 h irradiation with UV-vis light, the catalyst was removed from the reaction mixture and exposed to UV-vis light for another 24 h, yet with TEOA as sacrificial agent. Remarkably, no deactivation was observed in this case, in contrast to the experiment with the initial presence of TEOA (compare black and red line in Figure 1c).

The catalytic test results suggest that (i) the Pt cocatalyst is needed for effective H_2 formation over CN-based photocatalysts since it promotes electron transfer from the conduction band of CN to Pt and, thus, suppresses fast electron-hole recombination [20]; (ii) Composite formation of AIS with CN is detrimental for H_2 formation rates, yet it improves stability (iii) Despite the fact that AIS is able to absorb visible light (evidenced by UV-vis diffuse reflectance spectra, Figure S1) electron-hole separation and/or electron transfer might be inefficient and prevent proton reduction. (iv) The pH of the reaction solution has a significant impact on the stability of the Pt/CN catalyst. To elucidate

reasons for this different behavior, comprehensive catalyst characterization has been done, the results of which are described in the next section. Since Pt/10AIS-CN was revealed to be the best catalyst among the composites, it has been selected for comparison with Pt/CN in all further experiments.

2.2. Characterization of As-Prepared and Used Catalysts

Structural properties of the as-prepared photocatalysts are listed in Table 2. The band gap of CN decreases upon composite formation with AIS, suggesting that there is an effective interaction between AIS and CN in the composites (Figure S1). Surface area and pore volume pass a minimum for 10AIS-CN while the initial H_2 evolution rates within the first 4 h decrease with rising AIS content. This indicates that the BET surface area is not directly related to the photocatalytic activity. Similar observations were also made for a number of other photocatalysts based on heterojunctions of g-C_3N_4 with compounds such as Zn_2SnO_4 [21], $CdIn_2S_4$ [22], silver halides [23], $SmVO_4$ [24] or $CaIn_2S_4$ [11]. In these cases, enhanced photoactivities have been ascribed to improved stability of separated charge carriers and/or to improved light absorption in the composites. The lowest BET surface area of sample 10AIS-CN in Table 2 might result from a more effective surface coverage of CN by AIS than in the other composites.

Table 2. Structural properties of as-prepared (without deposited Pt) and used photocatalysts.

Catalyst	Band Gap (eV) [1]	S_{BET} (m^2/g)	Pore Volume (cm^3/g)	Mean Pore Size (nm)
CN	2.65	159.1	0.206	3.9
5AIS-CN	2.59	137.4	0.194	4.5
10AIS-CN	2.54	118.4	0.150	3.9
15AIS-CN	2.48	122.7	0.175	4.5
20AIS-CN	2.39	126.7	0.177	4.6
AIS	1.75	90.9	0.272	8.2
Pt/CN (20 h)	-	137.0	0.210	3.9

[1] derived from the absorption edges in the UV-vis-DR spectra (Figure S1b) using a Tauc plot [25].

The XRD powder pattern of CN shows a main peak at 2θ = 27.5° corresponding to the characteristic interlayer stacking reflection of polymeric melon sheets and a minor peak at 13.2° from an in-plane structural motif between nitride pores [26] (Figure S2a). Monophasic AIS gives rise to several peaks that can be assigned to the cubic face-centered lattice of this phase with a slight deviation of the unit cell parameters compared to reference [16] (ICDD 01-071-3985: 10.822 Å, found 10.797 Å) (Figure S2a). The XRD powder patterns of the Pt/CN and Pt/10AIS-CN samples removed from the catalytic reactor after 3 h and 20 h exposure to UV-vis light do not show any change of the CN and AIS reflections, suggesting that the bulk structure of these two phases remains stable during catalysis (Figure S2b). This has also been confirmed by ATR-IR spectra being identical for CN, 10AIS-CN as well as for Pt/CN and Pt/10AIS-CN after 3 h and 20 h use (Figure S3). The XRD powder patterns of the latter four catalysts show a small Pt(111) peak at 2θ = 39.9° which confirms the deposition of Pt particles as evidenced by scanning transmission electron microscopy with high angle annular dark field detector (STEM-HAADF), too (Figure 2).

Aberration corrected STEM-HAADF micrographs of Pt/CN removed from the reactor after 3 h (in the active state of the catalyst) show rather uniform Pt-containing particles of 5–10 nm size distributed on the surface of CN (Figure 2a, plots l and m). Besides, single Pt atoms are spread on the surface (Figure 2a, plot r). Interestingly, the Pt particle size and distribution remain almost unchanged in the Pt/CN catalysts after 20 h exposure to UV-vis light in the presence of TEOA (Figure 2b). This indicates that sintering of the Pt cocatalyst particles can be excluded as a reason for the observed catalyst deactivation (compare Figure 1a). However, it appeared that the CN phase in the sample used for 20 h is much more sensitive against beam damage than Pt/CN used for 3 h only. This suggests that prolonged exposure to UV-vis light causes changes in the electronic properties of the CN phase that may facilitate inclusion of Pt in the pores of CN, preventing them from participation in the reaction.

An indication for this was also obtained from XPS data (Table 1), in which a very low Pt surface content was observed for Pt/CN used with TEOA.

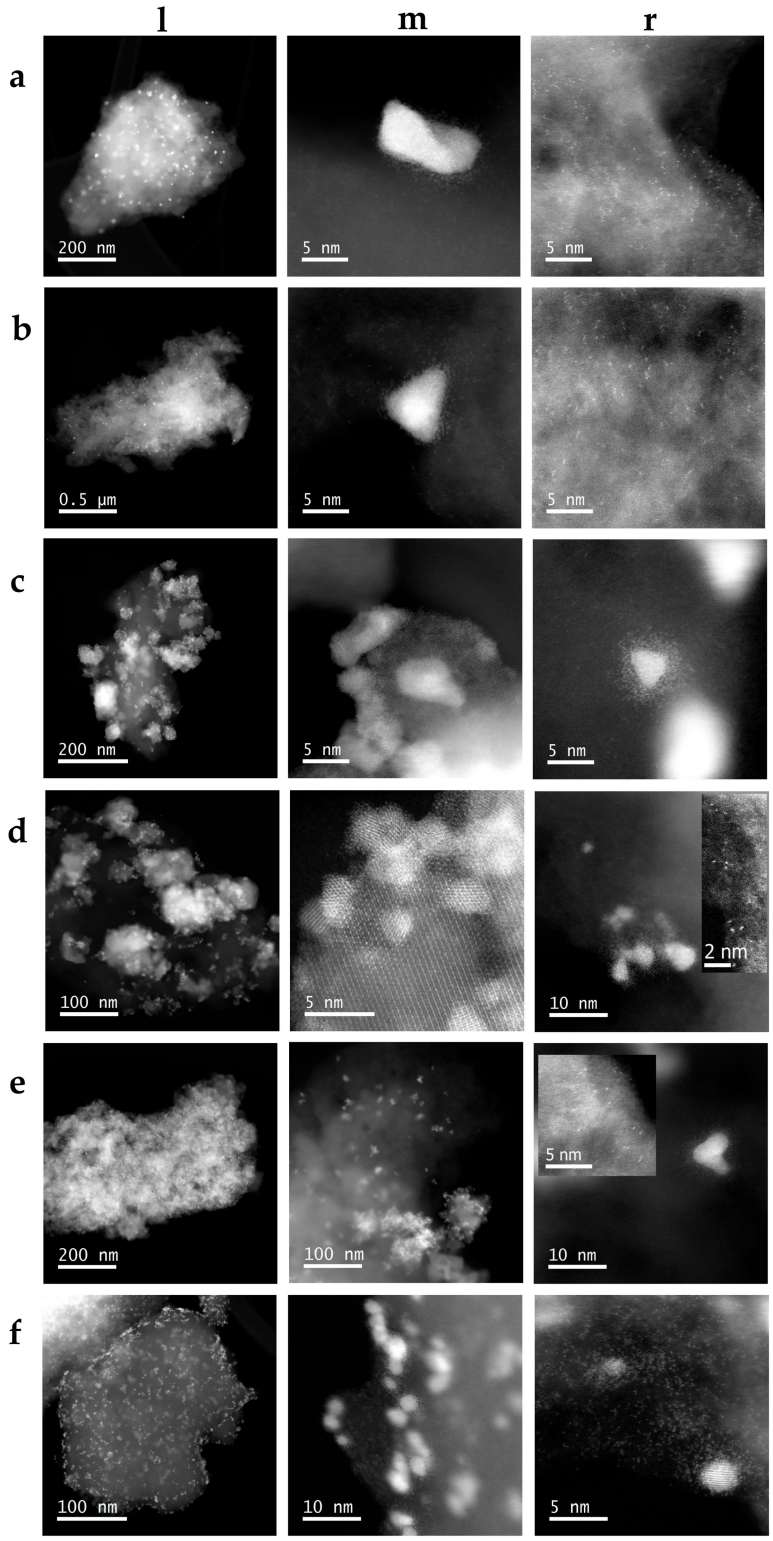

Figure 2. STEM-HAADF micrographs of catalysts exposed to UV-vis irradiation with TEOA: (**a**) Pt/CN for 3 h, (**b**) Pt/CN for 20 h, (**c**) Pt/10AIS-CN for 3 h, (**d**) Pt/10AIS-CN for 20 h, (**e**) physical mixture Pt/(10 wt.% AIS + CN) for 20 h and (**f**) Pt/CN after 4 h with oxalic acid (OA) as sacrificial agent. Plots l, m and r show areas of the same sample with different magnification.

In the much more stable catalyst Pt/10AIS-CN, Pt NPs of similar size as in Pt/CN are formed after 3 h which do also not change much after 20 h. However, the Pt NPs are preferentially deposited on the AIS phase (Figure 2c,d, plots l and m) which itself forms irregular particles of up to 100 nm in size (Figure 2c,d, plot m). On the CN phase, Pt particles are much less abundant while some single Pt atoms are also present (plot r). Thus, it appears that the AIS phase protects the Pt NPs against encapsulation in the CN phase, keeping them accessible to protons and active for photocatalysis. As mentioned above, the reason may be that the polar AIS surface enables adsorption and reduction of the polar $[PtCl_6]^{2-}$ precursor better than the non-polar CN surface, since the total Pt content of Pt/10AIS-CN after 3 h and 20 h use is close to the theoretical value (Table 1).

In the case of the physical mixture Pt/(10 wt.% AIS + CN) (Figure 2e), the Pt distribution is similar as in the Pt/10AIS-CN catalyst (Figure 2c,d). Some Pt single atoms are located on the CN phase while the Pt particles are enriched on the AIS particles. However, in the physical mixture, the CN and AIS phases do not exist as a tight composite but are separated from each other (Figure 2e, plot m). Since we have shown that Pt/AIS without contact to CN does not produce any H_2 (Figure 1a), it appears that catalytic activity and deactivation of the physical mixture Pt/(10 wt.% AIS + CN) is governed by the separately existing Pt/CN phase in this sample. This might be the reason why the catalytic behavior of samples Pt/(10 wt.% AIS + CN) and Pt/CN is so similar (compare Figure 1a).

When photocatalysis on Pt/CN is performed with oxalic acid instead of TEOA as sacrificial agent, Pt particles are located on the outermost surface of the CN phase where they remain accessible by protons (Figure 2f). This might be the reason for the high stability of the catalyst under these conditions (compare Figure 1c).

Since it may be expected that the surface of the catalysts experiences more significant changes than the bulk structure during catalysis, we performed XPS analyses of the catalysts removed from the reactor after 3 h (Pt/CN more active than Pt/10AIS-CN) and 20 h (Pt/10AIS-CN more active than Pt/CN) as well as from samples exposed to OA. The surface Pt content of the two Pt/CN samples is almost the same but about two orders of magnitude lower than the total Pt content determined by ICP-OES after 3 h and 20 h use (Table 1). This means that almost the whole Pt NPs seen by STEM-HAADF (Figure 2a,b) are enclosed in the matrix of CN. This is totally different for catalyst Pt/10AIS-CN after 3 h and 20 h use in which the surface Pt content is much higher than in AIS-free Pt/CN. This agrees well with STEM-HAADF results, which point to the preferential deposition of Pt on the AIS phase (Figure 2c,d). Moreover, the Ag:In:S atomic ratios in as-prepared 10AIS-CN and in the two Pt/10AIS-CN samples are close to the theoretical 1:5:8 ratio, suggesting that deposition-precipitation of the AIS component on the CN phase does not change composition and structure of the latter.

It has been shown by simultaneous in situ-SEM/STEM-HAADF analysis that Pt NPs deposited on the surface of carbon tend to migrate into the bulk of the support with rising temperature up to 200 °C, especially in the presence of air [27]. Possibly, a similar process is promoted at high pH in the Pt/CN samples. Note that the Pt surface content in sample Pt/CN_OA irradiated for 4 h in acidic medium is about 10 times higher than in Pt/CN treated for 3 h in TEOA. Thus, it appears that the AIS phase keeps Pt enriched and exposed on the catalyst surface. Interestingly, no deactivation was observed for sample Pt/CN (3 h) suggesting that, despite diffusion into the mesopores, the Pt NPs remain accessible to reactants during the initial 3 h of reaction. Only after more than 6 h reaction time, the Pt NPs lose their activity (Figure 1). In basic medium, formation of highly reactive $^{\cdot}OH$ radicals is expected by reaction of the holes with OH^- anions. We speculate that these species may attack the CN phase in the vicinity of the Pt NPs where they are formed, create defects and promote tight wrapping of the Pt NPs by CN. Remarkably, the BET surface area of catalyst Pt/CN after 20 h use is only slightly lower than that of the as-prepared CN phase while volume and mean diameter of the pores do not change at all (Table 2). This indicates, in agreement with ATR-IR and XRD results (Figures S2 and S3), that it might be a local densification of the CN phase around the Pt NPs, rather

than an extended collapse of surface and mesopore structure which reduces accessibility of Pt NPs by reactants. This aspect has been further analyzed by FTIR analysis of adsorbed CO (vide infra).

It seems that, the longer the exposure of Pt/CN to strongly basic medium, the higher is the danger of undesired support changes. Apart from the increased sensitivity of the CN phase against beam damage during STEM-HAADF (vide supra), this is supported, too, by the C 1s and N 1s XP spectra, which contain contributions from different moieties of the C_3N_4 structure [28] (Figure 3). Probably, a similar process takes place in Pt/10AIS-CN (20 h) as the CN phase in this sample was prone to beam damage in TEM as well. However, in this sample, Pt is enriched on the AIS phase which might protect it against inclusion in the CN pores. It can be seen from Figure 3b that the peak of N-(C_3) moieties decreases strongly upon prolonged irradiation in basic medium and the peak of C–N–H moieties disappears almost completely. On the other hand, the as-prepared CN catalyst contains a certain amount of oxygen, at least a part of which might account for the N=C–O moieties detected in Figure 3a. These disappeared during use in the reaction, too. Considering the position of such moieties within the C_3N_4 structure (Figure 3d), it seems probable that their removal leaves behind defects that could support local changes (densification) of the CN structure around the Pt NPs, which in turn shields the latter against contact to reactants.

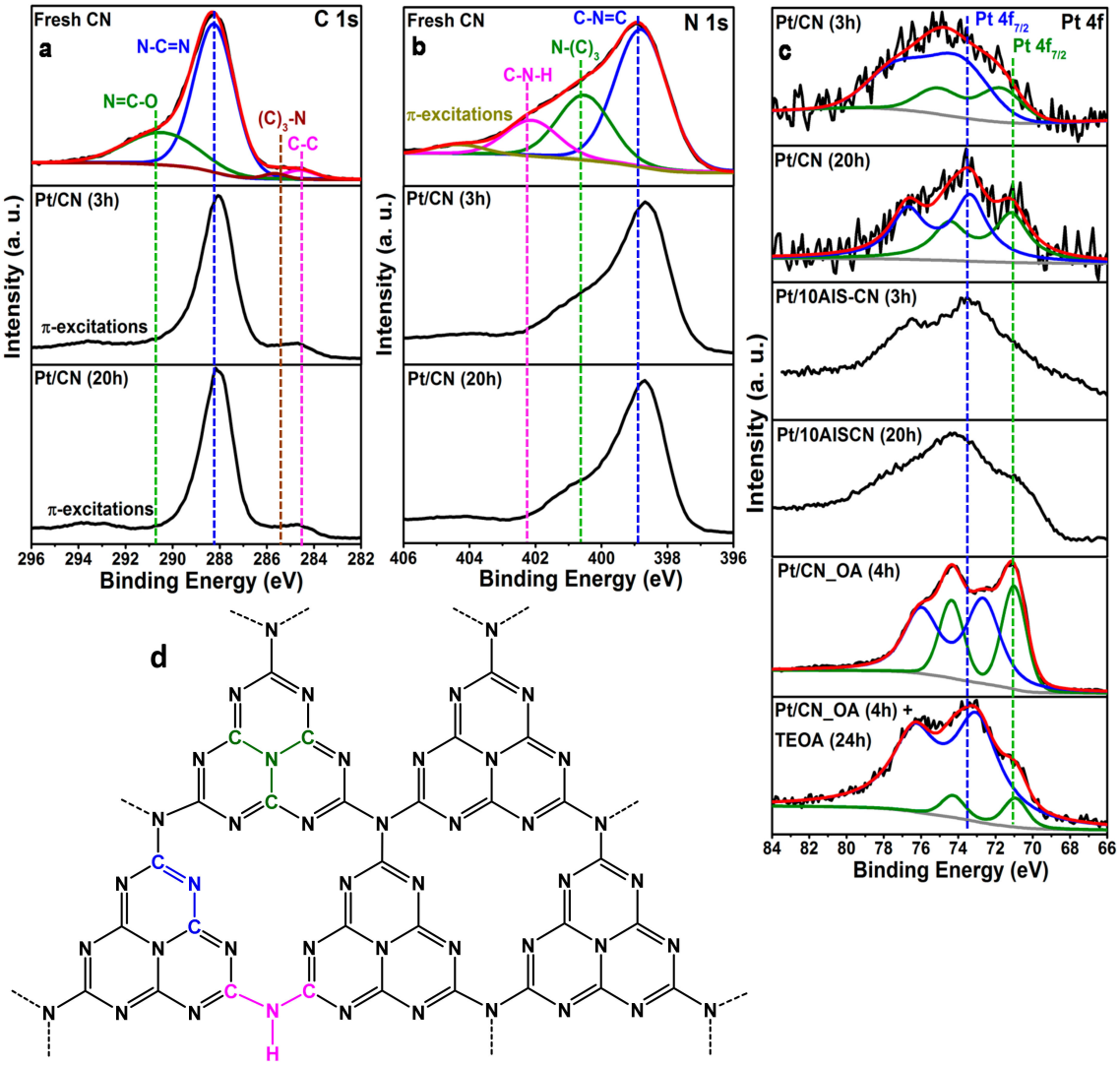

Figure 3. XP spectra of selected samples in the C 1s (**a**), N 1s (**b**) and Pt 4f region (**c**) blue: Pt^{2+}, green: Pt^0 together with a scheme of the C_3N_4 structure (**d**).

The surface composition of the Pt NPs in the various catalysts treated in TEOA does not differ much. All NPs contain metallic Pt^0 besides oxidized Pt^{2+}, reflected by Pt $4f_{7/2}$ peaks at 70–72 eV and 74 eV, respectively [19] (Figure 3c). Especially in the AIS-containing samples, these peaks are very broad, making a meaningful deconvolution into distinct doublets for $4f_{7/2}$ and $4f_{5/2}$ difficult. The reason might be the simultaneous presence of Pt species in different environment (evidenced by STEM-HAADF, Figure 2c,d), e.g., single atoms, small particles and agglomerates of small particles in the vicinity of both CN as well as AIS.

When Pt NPs are deposited in situ on CN in the presence of OA, the Pt surface percentage is much higher compared to TEOA (0.85 at.% vs. 0.06 at.%, Table 1), since the particles are located preferentially on the outer surface of CN (Figure 2f). However, also in this case Pt^0 and Pt^{2+} coexist on the surface (Figure 3c, green and blue fitted lines). After subsequent treatment of Pt/CN_OA (4 h) under UV-vis light in TEOA for 24 h, the Pt^{2+} is even more dominating on the surface than in sample Pt/CN (20 h) treated only in TEOA (compare Figure 3c, bottom plots). This confirms again that the enrichment of oxidic Pt on the NP surface is no reason for deactivation, since the latter catalyst does not deactivate (compare Figure 1c).

The accessibility of the active Pt species has been investigated by FTIR analysis of adsorbed CO (Figure 4). Bands of CO adsorbed on oxidized Pt^{2+}/Pt^{+} as well as on metallic Pt^0 can be seen in Figure 4 [29], in agreement with XPS results showing contributions of both oxidized and zerovalent Pt species, too (compare Figure 3c). The band intensities of all species drop significantly after exposure of Pt/CN to the photocatalytic reaction for 20 h, indicating clearly that the accessibility of the Pt surface for reactants decreases, too. This might explain the observed strong deactivation of catalyst Pt/CN after 20 h (Figure 1).

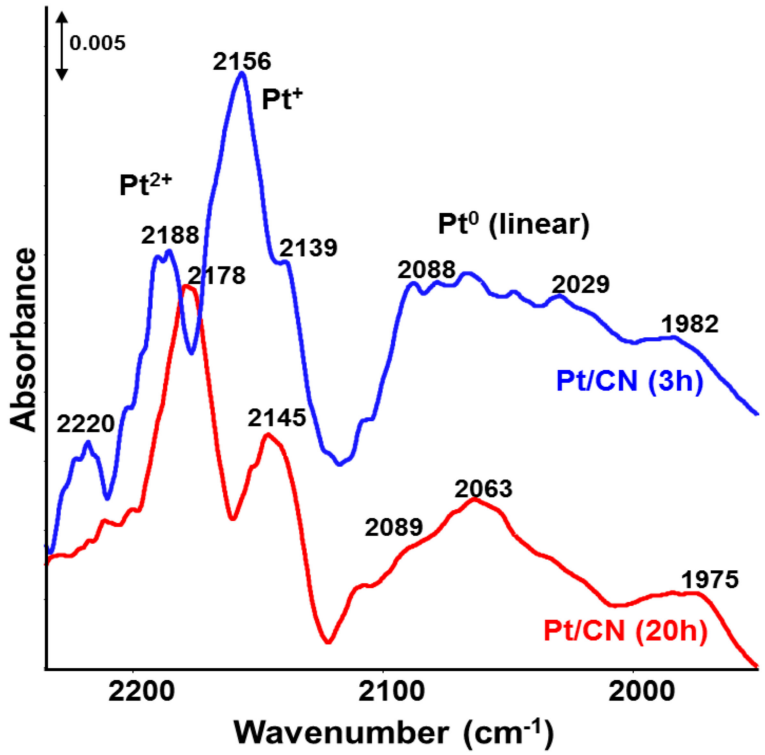

Figure 4. FTIR spectra of adsorbed CO for catalyst Pt/CN after 3 h and 20 h use in the reaction with UV-vis light.

2.3. Charge Separation and Transfer

In situ-EPR is a versatile technique to monitor separation and transfer of photogenerated electrons in semiconductors based on oxides [30] or carbon nitrides [20], since electrons excited to the conduction

band (CB-e^-) can be trapped at oxygen vacancies [30] and carbon defects [24]. All as-prepared CN-containing catalysts show a narrow isotropic singlet with Lorentzian line shape at g = 2.0042 already in the dark (not shown) arising from single electrons trapped at a surface sp^2-carbon in a typical heptazine unit [31,32]. Note that the conduction band of CN is formed by C 2p orbitals, while the valence band is mainly made up of N 2p orbitals [5]. This signal increases during irradiation with UV-vis light, due to electron-hole separation and excitation of electrons into the CN conduction band and decreases again when the light is switched off, due to charge carrier recombination (Figure 5a). The EPR signal under UV-light irradiation is highest for pure CN and decreases with rising AIS content in the composites. This is most probably due to transfer of electrons from the CN conduction band to AIS in the composites (Figure 5b). Another indication for such a process is provided by photoluminescence (PL) spectra (vide infra).

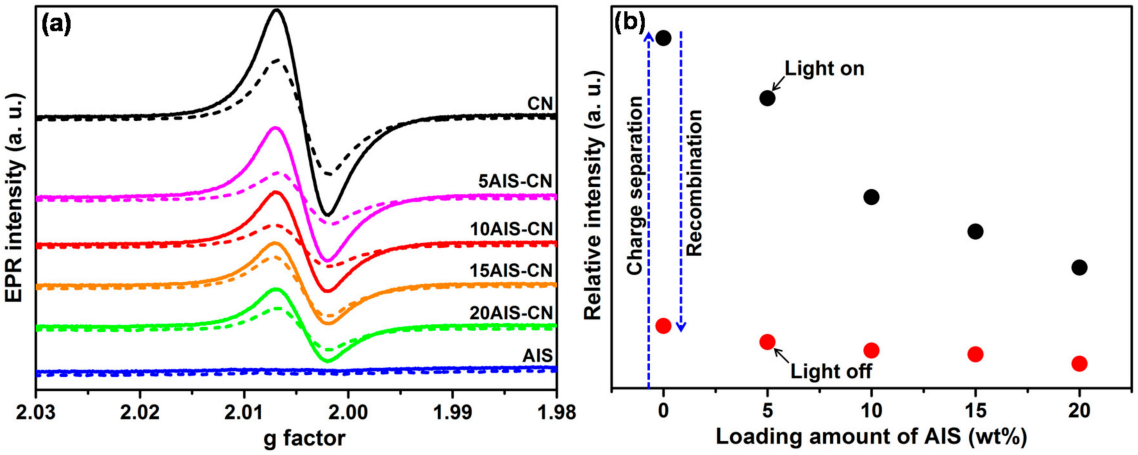

Figure 5. (**a**) Electron paramagnetic resonance (EPR) signal of CB-e^- in as-prepared catalysts (without Pt) during UV-vis irradiation (solid lines) and after light switched-off (dashed lines); (**b**) Double integral of the EPR CB e-signal intensity (initial background signal in the dark subtracted) during UV-vis light irradiation (black dots) and after light switched-off (red dots).

As mentioned in Section 2.1, neither CN nor the AIS-CN composites are active in H_2 production without Pt NPs as cocatalyst. This suggests that further transfer of separated CB-e^- via AIS to Pt or, in the case of monophasic CN, directly to Pt NPs, is essential to guarantee a charge carrier lifetime long enough for reaction with protons. The effect of deposited Pt NPs is also evident from in situ-EPR spectra of samples Pt/CN and Pt/10AIS-CN removed from the photocatalytic reactor after 3 h and 20 h use under UV-vis irradiation (Figure 5).

In comparison to the as-prepared samples without Pt, the deposition of Pt NPs leads to a drop of the CB-e^- EPR signal, indicating that those electrons are transferred to Pt from which they react with protons to produce H_2 [20]. Interestingly, the EPR intensity under UV-vis irradiation (Figure 6) seems to reflect somehow the catalytic behavior (compare Figure 1a). It is higher for Pt/CN after 20 h (deactivated) than after 3 h (still active), while it remains almost equal and rather low for Pt/10AIS-CN which shows negligible deactivation. Obviously, in active catalysts fast transfer of CB-e^- via CN $\rightarrow$ (AIS) $\rightarrow$ Pt $\rightarrow$ H^+ $\rightarrow$ H_2 takes place, keeping the CB-e^- electron signal small, while the Pt $\rightarrow$ H^+ $\rightarrow$ H_2 step of this chain might be hindered in less active catalysts, leading to higher EPR intensity.

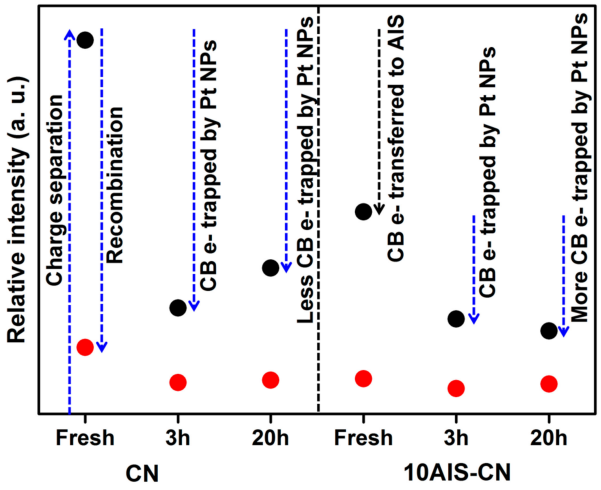

Figure 6. Intensity (double integral) of the CB-e-EPR signal (initial background signal in the dark substracted) during UV-vis light irradiation (black dots) and after light switched-off (red dots). Values for as-prepared samples without Pt (fresh) taken from Figure 5b.

Interesting information on charge separation and transfer can also be obtained from PL spectra (Figure 7). PL radiation is emitted as consequence of electron-hole pair recombination, yet the intensity of the PL depends on the lifetime of the separated charges. Higher PL intensities have been observed for photocatalysts with longer charge carrier lifetime [33]. From Figure 7a it is evident that the highest PL signal appears for pure CN while pure AIS gives no PL, despite the fact that it absorbs UV-vis light able to excite electrons from the valence to the conduction band (compare Figure S1). This suggests that electron-hole recombination in the pure AIS phase might be too fast to emit PL radiation. With rising percentage of AIS, the intensity of PL from the CN phase decreases, most probably due to fast transfer of the excited electrons from the conduction band of CN to that of AIS. A similar effect was also observed for other C_3N_4-based photocatalysts such as In_2S_3/g-C_3N_4 [34], $ZnFe_2O_4$/g-C_3N_4 [35], $Cu_2O/NaTaO_3$ [36], g-C_3N_4/NiFe-LDH [37] and MoS_2/g-C_3N_4 [38]. When Pt is deposited on both, pure CN and the 10AIS-CN composite, giving rise to photocatalytic activity, the PL signal decreases (Figure 7b). The reason might be transfer of excited CB electrons from CN to Pt or from CN via AIS to Pt, respectively, which efficiently prevents charge carrier recombination and extends their lifetime sufficiently for reduction of protons to H_2. On the other hand, the reason for the decreasing H_2 evolution rates with rising AIS content in the AIS-CN composites may be AIS mediated quenching of a part of the CB e^- before they reach the Pt conduction band.

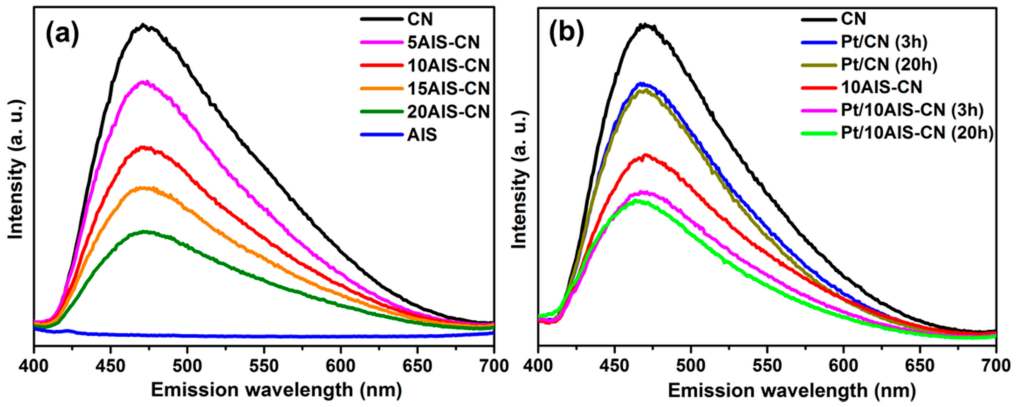

Figure 7. Photoluminescence spectra of as-prepared catalysts without Pt (**a**) and Pt containing catalysts after 3 h and 20 h use under UV-vis irradiation (**b**) For comparison the Pt free supports are shown in plot b as well.

3. Materials and Methods

3.1. Catalyst Synthesis

Mesoporous C_3N_4 (CN) has been synthesized by a hard template method described in detail previously [14]. Briefly, cyanamide (CA) was dissolved in a mixed solution of ethanol and HCl at pH = 2. After adding tetraethylorthosilicate (TEOS) the mixture was stirred for 30 min, followed by evaporation of the solvent and drying at 80 °C. Afterwards, the dry solid was subjected to a stepwise thermal treatment at 550 °C in argon and at 650 °C in ambient atmosphere. Finally, the formed silica was removed from the composite by treatment with a 4 M NH_4HF_2 solution to create mesopores.

$AgIn_5S_8$ (AIS) nanoparticles were synthesized by a co-precipitation method [16]. Typically, 0.0680 g (0.4 mmol) of $AgNO_3$ and 0.7818 g (2.0 mmol) of $In(NO_3)_3{\cdot}5H_2O$ were dispersed in 120 mL double distilled water under vigorous stirring for 30 min. Then, 0.6010 g (8.0 mmol) of thioacetamide (C_2H_5NS) was added to the above reaction mixture. Subsequently, the reaction mixture was kept on an oil bath at 60 °C for 12 h under magnetic stirring (300 rpm) with a condenser. The resulting grey colored precipitate was filtered, washed with distilled water and ethanol for several times and then dried for 12 h at 80 °C in ambient atmosphere.

AIS-CN composites with different AIS content (labelled as xAIS-CN, where x denotes the weight percentage of AIS) were synthesized by performing the above described co-precipitation in the presence of CN. In a typical synthesis procedure, 0.1800 g of CN was dispersed in 20 mL double distilled water by vigorous stirring for 30 min. To obtain a composite with 10 wt.% AIS, 0.0036 g of $AgNO_3$ and 0.0417 g of $In(NO_3)_3{\cdot}5H_2O$ were added to this suspension and vigorously stirred for 30 min. After adding 0.0321 g of thioacetamide (C_2H_5NS) the mixture was stirred at 60 °C for 12 h. The resulting yellow-grey colored precipitate was filtered, washed and dried in the same way as pure AIS. To obtain composites with 5%, 15% and 20% AIS, the concentrations of the respective precursors have been adjusted accordingly.

3.2. Catalyst Characterization

XRD powder patterns were recorded either on a X'Pert diffractometer (Panalytical, Almelo, The Netherlands) equipped with a Xcelerator detector or on a Panalytical Empyrean diffractometer equipped with a PIXcel 3D detector system (Panalytical, Almelo, The Netherlands) both used with automatic divergence slits and Cu kα1/α2 radiation (40 kV, 40 mA; λ = 0.015406 nm, 0.0154443 nm). Cu beta-radiation was excluded by using a nickel filter foil. The measurements were performed in 0.0167° steps and 25 s of data collecting time per step. Peak positions and profile were fitted with pseudo-Voigt function using the HighScore Plus software package (V. 3.0e, Panalytical, Almelo, The Netherlands). Phase identification was done by using the PDF-2 database of the International Center of Diffraction Data (ICDD).

Diffuse reflectance UV-vis spectra were obtained by a Cary5000 spectrometer (Agilent Technologies Inc., Mulgrave, Australia) equipped with a diffuse reflectance accessory (Praying Mantis^{TM}, Harrick Scientific Products, Inc., Pleasantville, NY, USA) by using $BaSO_4$ as white standard reference material.

IR spectra in attenuated total reflectance mode (ATR-IR) were recorded on a Nicolet iS10 Instrument (Thermo Fisher Scientific Inc., Madison, WI, USA). For the characterization of exposed Pt species, CO was used as probe molecule. These measurements were carried out in transmission mode on a Bruker Tensor 27 FTIR spectrometer equipped with a heatable and evacuable homemade reaction cell with CaF_2 windows connected to a gas-dosing and evacuation system. The sample powders were pressed into self-supporting wafers with a diameter of 20 mm and a weight of 50 mg. Before CO adsorption, the samples were pretreated by heating at 100 °C under vacuum for 30 min. CO (5% CO/He) was adsorbed at room temperature until saturation. Then the reaction cell was evacuated, and the CO adsorbate spectrum was recorded. Generally, the spectrum of the catalyst measured after pretreatment at room temperature was subtracted from the respective adsorbate spectra.

Photoluminescence (PL) spectra were obtained by a Cary Eclipse Fluorescence spectrophotometer (Agilent Technologies Inc., Mulgrave, Australia) with an excitation wavelength of 370 nm.

STEM-HAADF micrographs were obtained at 200 kV by a probe aberration corrected JEM-ARM200F transmission electron microscope (Jeol Ltd., Akishima, Japan). The microscope is equipped with a JED-2300 (JEOL) energy dispersive X-ray spectrometer (EDXS) for chemical analysis. The catalyst powder was dry deposited on a Cu grid (mesh 300) covered by a holey carbon film and transferred into the microscope.

X-ray photoelectron spectra were performed by a Thermo ESCALAB 220 iXL spectrometer (Thermo Fisher Scientific, Inc., Waltham, MA, USA) at room temperature using monochromatic AlKα radiation. Binding energies were corrected to C–C contribution at 284.8 eV in C 1s region. Signal intensities were normalized using the sensitivity factors of Scofield [39] and the transmission function of the spectrometer.

BET surface areas and pore properties (Figure S4) were determined by standard nitrogen adsorption at −196 °C (ASAP 2020, Micromeritics GmbH, Aachen, Germany).

The elemental bulk composition was determined using a Varian 715-ES ICP-emission spectrometer (Varian Deutschland GmbH, Darmstadt, Germany) and the Varian 720-ES Instrument software (Version 1.1, Varian Deutschland GmbH, Darmstadt, Germany).

3.3. In-Situ Electron Paramagnetic Resonance Spectroscopy Studies

In situ-EPR measurements in X-band (microwave frequency ≈ 9.8 GHz) were performed at 300 K by an EMX CW-micro spectrometer (Bruker Biospin GmbH, Rheinstetten, Germany) equipped with an ER 4119HS-WI high-sensitivity optical resonator with a grid in the front side (Bruker Biospin GmbH, Rheinstetten, Germany). The samples were illuminated by a 300 W Xe lamp (LOT-QuantumDesign GmbH, Darmstadt, Germany). All the samples were measured under the same conditions (microwave power: 6.99 mW, receiver gain: 1×10^4, modulation frequency: 100 kHz, modulation amplitude: 3 G, Sweep time: 122.8 s). g values have been calculated from the resonance field B_0 and the resonance frequency ν using the resonance condition $h\nu = g\beta B_0$. The calibration of the g values was performed using DPPH (2,2-diphenyl-1-picrylhydrazyl) ($g = 2.0036 \pm 0.00004$).

3.4. Photocatalytic Hydrogen Evolution Tests

All catalytic experiments were carried out under an argon atmosphere with distilled solvents. Catalytic tests were performed in a double walled and thermostatically controlled reaction vessel connected to an automatic gas burette (Figure S5). Before each experiment, the reactor was several times evacuated and filled with argon to remove air. In a typical experiment, the reactor was charged with 24.5 mg of catalyst and 0.2 mL aqueous $H_2PtCl_6 \cdot xH_2O$, containing 0.5 mg Pt to achieve a nominal Pt loading of 2 wt.% Pt. Then 24.8 mL of a mixture of water and triethanolamine (TEOA, used as sacrificial agent) were added to obtain a final ratio of water/TEOA of 9/1 (v/v), and the temperature was maintained at 25 °C. After stirring for approximately 10 min to reach thermal equilibrium the reaction was started by switching the light source on. As light source a 300 W Xe lamp with an output power of 1.5 W was used. For working under visible light irradiation only, a 420 nm cut-off filter was applied. The amounts of evolved gases were continuously determined by the automatic gas burette, equipped with a pressure sensor. After each experiment, a 5 mL gas sample was taken from the burette and quantitatively analyzed by a GC HP 6890N gas chromatograph (Agilent Technologies Inc., Wilmington, DE, USA) equipped with a carboxen 1000 column and a thermal conductivity detector (TCD) and Ar as carrier gas. In selected experiments, the reaction was stopped after 3 h or 20 h, respectively, the catalyst was recovered by centrifugation, washed with double distilled water and ethanol and dried overnight at room temperature for further characterization.

4. Conclusions

Pt/CN composites without AIS showed highest initial H_2 evolution rates in both basic (TEOA) and acidic (OA) aqueous solutions. However, in basic medium (pH = 10.6), Pt NPs are encapsulated in the bulk structure of CN, leading to fast deactivation within the first 4–6 h of the photocatalytic reaction under UV-vis light, which occurs, though slower, under pure visible light ($\lambda \geq 420$ nm), too. The reason may be an attack of the CN structure by highly reactive $^{\cdot}$OH radicals leading to defect formation and subsequent densification. With increasing percentage of AIS in the Pt/xAIS-CN ($0 \leq x \leq 20$ wt.%) composites, the initial H_2 evolution rates decrease, while Pt/AIS without CN was completely inactive. This suggests that, though AIS does absorb visible light and should undergo electron-hole separation as well, charge recombination within this phase is obviously very fast (suggested by missing photoluminescence). This prevents electron transfer from the AIS conduction band to the Pt particles. In composites of AIS with CN, electrons excited from the valence to the conduction band of CN travel through the interface to AIS and further to the Pt particles, which are enriched preferentially on the AIS surface. This transfer is only possible when an effective heterojunction exists. This must be concluded since the course in catalytic activity of a physical mixture of CN and AIS (with no such heterojunction) is similar to Pt/CN without AIS (Figure 1a) and Pt/AIS is not active at all. Apparently, an optimum situation results for sample Pt/10AIS-CN, in which the CN surface is obviously covered most effectively by AIS particles (indicated by the lowest BET surface area, Table 2), while these particles might be still thin enough to enable effective transfer of CB-e^- from CN via AIS to Pt where they reduce protons to hydrogen. The same process happens in aqueous oxalic acid solution (pH = 0.67), though H_2 formation rates are generally higher due to the higher proton concentration.

The main difference resulting from the pH of the reaction solution concerns catalyst stability which is related to the nature of the Pt NPs. The Pt surface consists of both metallic Pt^0 and oxidic Pt^{2+} in all cases, which excludes partial oxidation of metallic Pt as reason for the fast deactivation of the Pt/CN catalyst. However, in acidic medium (pH = 0.67), Pt NPs in Pt/CN remain active since they are exposed on the outer surface of the CN phase and not encapsulated in the CN bulk structure, like in basic medium (pH = 10.6).

Supplementary Materials: The following data are available online at http://www.mdpi.com/2073-4344/8/2/52/s1, Table S1: Surface area, reaction conditions and H_2 evolution rates of selected C_3N_4-based photocatalysts, Table S2: Reaction conditions and H_2 evolution rates of $AgIn_5S_8$ photocatalysts, Figure S1: (a) UV-vis-DR spectra of AIS, CN and AIS-CN composites with different contents of AIS; (b) Band gap estimation from Tauc plot, Figure S2: XRD powder patterns of (a) as-prepared samples and (b) Pt/CN and Pt/10AIS-CN samples removed from the reactor after 3 and 20 h irradiation with UV-vis light in the presence of TEOA, Figure S3: ATR-IR spectra of (a) as-prepared samples and (b) Pt/CN and Pt/10AIS-CN samples removed from the reactor after 3 and 20 h irradiation with UV-vis light in the presence of TEOA, Figure S4: N_2 adsorption-desorption isotherms of AIS, CN and 10AIS-CN; (b) Barrett-Joyner-Halenda pore size distribution plot. N_2 adsorption-desorption revealed type IV isotherms for both CN and 10AIS-CN, indicating the presence of slit-shaped mesopores (2–50 nm). In contrast, AIS is a nonporous powder. The pore size distributions of the samples were estimated by the Barrett-Joyner-Halenda (BJH) method from the desorption branches (plot b), Figure S5: Photocatalytic test setup.

Acknowledgments: The authors thank R. Eckelt for performing N_2 adsorption measurements.

Author Contributions: Ramesh P. Sivasankaran prepared catalysts and performed catalytic tests, Nils Rockstroh, Dirk Hollmann and Jabor Rabeah supported catalytic tests, EPR measurements and contributed to the discussions; Carsten R. Kreyenschulte, Giovanni Agostini, Henrik Lund and Ursula Bentrup performed and evaluated STEM-HAADF, XPS, XRD and ATR-IR experiments, respectively; Amitava Acharjya and Arne Thomas provided CN materials; Henrik Junge provided the catalytic test setup, Angelika Brückner wrote the manuscript.

Conflicts of Interest: The authors declare no conflict of interest.

References

1. Armaroli, N.; Balzani, V. The Future of Energy Supply: Challenges and Opportunities. *Angew. Chem. Int. Ed.* **2007**, *46*, 52–66. [CrossRef] [PubMed]
2. Lewis, N.S.; Nocera, D.G. Powering the planet: Chemical challenges in solar energy utilization. *Proc. Natl. Acad. Sci. USA* **2006**, *103*, 15729–15735. [CrossRef] [PubMed]

3. Takanabe, K.; Domen, K. Preparation of Inorganic Photocatalytic Materials for Overall Water Splitting. *ChemCatChem* **2012**, *4*, 1485–1497. [CrossRef]
4. Kudo, A.; Miseki, Y. Heterogeneous photocatalyst materials for water splitting. *Chem. Soc. Rev.* **2009**, *38*, 253–278. [CrossRef] [PubMed]
5. Wang, X.; Maeda, K.; Thomas, A.; Takanabe, K.; Xin, G.; Carlsson, J.M.; Domen, K.; Antonietti, M. A metal-free polymeric photocatalyst for hydrogen production from water under visible light. *Nat. Mater.* **2009**, *8*, 76–80. [CrossRef] [PubMed]
6. Ye, C.; Li, J.-X.; Li, Z.-J.; Li, X.-B.; Fan, X.-B.; Zhang, L.-P.; Chen, B.; Tung, C.-H.; Wu, L.-Z. Enhanced Driving Force and Charge Separation Efficiency of Protonated g-C_3N_4 for Photocatalytic O_2 Evolution. *ACS Catal.* **2015**, *5*, 6973–6979. [CrossRef]
7. Zhang, S.; Li, J.; Wang, X.; Huang, Y.; Zeng, M.; Xu, J. Rationally designed 1D Ag@$AgVO_3$ nanowire/graphene/protonated g-C_3N_4 nanosheet heterojunctions for enhanced photocatalysis via electrostatic self-assembly and photochemical reduction methods. *J. Mater. Chem. A* **2015**, *3*, 10119–10126. [CrossRef]
8. Ong, W.-J.; Tan, L.-L.; Ng, Y.H.; Yong, S.-T.; Chai, S.-P. Graphitic Carbon Nitride (g-C_3N_4)-Based Photocatalysts for Artificial Photosynthesis and Environmental Remediation: Are We a Step Closer to Achieving Sustainability? *Chem. Rev.* **2016**, *116*, 7159–7329. [CrossRef] [PubMed]
9. Yin, S.; Han, J.; Zhou, T.; Xu, R. Recent progress in g-C_3N_4 based low cost photocatalytic system: Activity enhancement and emerging applications. *Catal. Sci. Technol.* **2015**, *5*, 5048–5061. [CrossRef]
10. Zheng, Y.; Lin, L.; Wang, B.; Wang, X. Graphitic Carbon Nitride Polymers toward Sustainable Photoredox Catalysis. *Angew. Chem. Int. Ed.* **2015**, *54*, 12868–12884. [CrossRef] [PubMed]
11. Jiang, D.; Li, J.; Xing, C.; Zhang, Z.; Meng, S.; Chen, M. Two-Dimensional $CaIn_2S_4$/g-C_3N_4 Heterojunction Nanocomposite with Enhanced Visible-Light Photocatalytic Activities: Interfacial Engineering and Mechanism Insight. *ACS Appl. Mater. Interfaces* **2015**, *7*, 19234–19242. [CrossRef] [PubMed]
12. Liu, H.; Xu, Z.; Zhang, Z.; Ao, D. Highly efficient photocatalytic H_2 evolution from water over $CdLa_2S_4$/mesoporous g-C_3N_4 hybrids under visible light irradiation. *Appl. Catal. B Environ.* **2016**, *192*, 234–241. [CrossRef]
13. Zhang, Z.; Liu, K.; Feng, Z.; Bao, Y.; Dong, B. Hierarchical Sheet-on-Sheet $ZnIn_2S_4$/g-C_3N_4 Heterostructure with Highly Efficient Photocatalytic H_2 production Based on Photoinduced Interfacial Charge Transfer. *Sci. Rep.* **2016**, *6*, 19221–19231. [CrossRef] [PubMed]
14. Kailasam, K.; Epping, J.D.; Thomas, A.; Losse, S.; Junge, H. Mesoporous carbon nitride-silica composites by a combined sol-gel/thermal condensation approach and their application as photocatalysts. *Energy Environ. Sci.* **2011**, *4*, 4668–4674. [CrossRef]
15. Lennox, A.J.J.; Bartels, P.; Pohl, M.M.; Junge, H.; Beller, M. In situ photodeposition of copper nanoparticles on TiO_2: Novel catalysts with facile light-induced redox cycling. *J. Catal.* **2016**, *340*, 177–183. [CrossRef]
16. Li, K.; Xu, J.; Zhang, X.; Peng, T.; Li, X. Low-temperature preparation of $AgIn_5S_8$/TiO_2 heterojunction nanocomposite with efficient visible-light-driven hydrogen production. *Int. J. Hydrogen Energy* **2013**, *38*, 15965–15975. [CrossRef]
17. Li, K.; Chai, B.; Peng, T.; Mao, J.; Zan, L. Preparation of $AgIn_5S_8$/TiO_2 Heterojunction Nanocomposite and Its Enhanced Photocatalytic H_2 Production Property under Visible Light. *ACS Catal.* **2013**, *3*, 170–177. [CrossRef]
18. Chen, D.; Ye, J. Photocatalytic H_2 evolution under visible light irradiation on $AgIn_5S_8$ photocatalyst. *J. Phys. Chem. Solids* **2007**, *68*, 2317–2320. [CrossRef]
19. Zhang, F.; Chen, J.; Zhang, X.; Gao, W.; Jin, R.; Guan, N.; Li, Y. Synthesis of Titania-Supported Platinum Catalyst: The Effect of pH on Morphology Control and Valence State during Photodeposition. *Langmuir* **2004**, *20*, 9329–9334. [CrossRef] [PubMed]
20. Hollmann, D.; Karnahl, M.; Tschierlei, S.; Kailasam, K.; Schneider, M.; Radnik, J.; Grabow, K.; Bentrup, U.; Junge, H.; Beller, M.; et al. Structure-Activity Relationships in Bulk Polymeric and Sol-Gel-Derived Carbon Nitrides during Photocatalytic Hydrogen Production. *Chem. Mater.* **2014**, *26*, 1727–1733. [CrossRef]
21. Zhang, L.; Wang, X.; Nong, Q.; Lin, H.; Teng, B.; Zhang, Y.; Zhao, L.; Wu, T.; He, Y. Enhanced visible-light photoactivity of g-C_3N_4 via Zn_2SnO_4 modification. *Appl. Surf. Sci.* **2015**, *329*, 143–149. [CrossRef]

22. Chen, W.; Huang, T.; Hua, Y.-X.; Liu, T.-Y.; Liu, X.-H.; Chen, S.-M. Hierarchical $CdIn_2S_4$ microspheres wrapped by mesoporous g-C_3N_4 ultrathin nanosheets with enhanced visible light driven photocatalytic reduction activity. *J. Hazard. Mater.* **2016**, *320*, 529–538. [CrossRef] [PubMed]
23. Xu, H.; Yan, J.; Xu, Y.; Song, Y.; Li, H.; Xia, J.; Huang, C.; Wan, H. Novel visible-light-driven AgX/graphite-like C_3N_4 (X = Br, I) hybrid materials with synergistic photocatalytic activity. *Appl. Catal. B Environ.* **2013**, *129*, 182–193. [CrossRef]
24. Li, T.; Zhao, L.; He, Y.; Cai, J.; Luo, M.; Lin, J. Synthesis of g-C_3N_4/$SmVO_4$ composite photocatalyst with improved visible light photocatalytic activities in RhB degradation. *Appl. Catal. B Environ.* **2013**, *129*, 255–263. [CrossRef]
25. Nashim, A.; Martha, S.; Parida, K.M. Heterojunction conception of n-$La_2Ti_2O_7$/p-CuO in the limelight of photocatalytic formation of hydrogen under visible light. *RSC Adv.* **2014**, *4*, 14633–14643. [CrossRef]
26. Tyborski, T.; Merschjann, C.; Orthmann, S.; Yang, F.; Lux-Steiner, M.C.; Schedel-Niedrig, T. Crystal structure of polymeric carbon nitride and the determination of its process-temperature-induced modifications. *J. Phys. Condens. Matter* **2013**, *25*, 395402–395408. [CrossRef] [PubMed]
27. Isakozawa, S.; Nagaoki, I.; Watabe, A.; Nagakubo, Y.; Saito, N.; Matsumoto, H.; Zhang, X.F.; Taniguchi, Y.; Baba, N. Design of a 300-kV gas environmental transmission electron microscope equipped with a cold field emission gun. *Microsc. Anal.* **2016**, *65*, 353–362. [CrossRef] [PubMed]
28. Indra, A.; Acharjya, A.; Menezes, P.W.; Merschjann, C.; Hollmann, D.; Schwarze, M.; Aktas, M.; Friedrich, A.; Lochbrunner, S.; Thomas, A.; et al. Boosting Visible-Light-Driven Photocatalytic Hydrogen Evolution with an Integrated Nickel Phosphide-Carbon Nitride System. *Angew. Chem.* **2017**, *129*, 1675–1679. [CrossRef]
29. Davydov, A. *Molecular Spectroscopy of Oxide Catalyst Surfaces*; John Wiley & Sons Ltd.: Chichester, UK, 2003; pp. 238–252.
30. Priebe, J.B.; Radnik, J.; Lennox, A.J.J.; Pohl, M.-M.; Karnahl, M.; Hollmann, D.; Grabow, K.; Bentrup, U.; Junge, H.; Beller, M.; et al. Solar Hydrogen Production by Plasmonic Au-TiO_2 Catalysts: Impact of Synthesis Protocol and TiO_2 Phase on Charge Transfer Efficiency and H_2 Evolution Rates. *ACS Catal.* **2015**, *5*, 2137–2148. [CrossRef]
31. Zhang, J.; Zhang, G.; Chen, X.; Lin, S.; Mohlmann, L.; Dolega, G.; Lipner, G.; Antonietti, M.; Blechert, S.; Wang, X. Co-monomer control of carbon nitride semiconductors to optimize hydrogen evolution with visible light. *Angew. Chem. Int. Ed.* **2012**, *51*, 3183–3187. [CrossRef] [PubMed]
32. Priebe, J.B.; Karnahl, M.; Junge, H.; Beller, M.; Hollmann, D.; Bruckner, A. Water reduction with visible light: Synergy between optical transitions and electron transfer in Au-TiO_2 catalysts visualized by in situ EPR spectroscopy. *Angew. Chem. Int. Ed.* **2013**, *52*, 11420–11424. [CrossRef] [PubMed]
33. Miyashita, K.; Kuroda, S.-I.; Tajima, S.; Takehira, K.; Tobita, S.; Kubota, H. Photoluminescence study of electron-hole recombination dynamics in the vacuum-deposited SiO_2/TiO_2 multilayer film with photo-catalytic activity. *Chem. Phys. Lett.* **2003**, *369*, 225–231. [CrossRef]
34. Xing, C.; Wu, Z.; Jiang, D.; Chen, M. Hydrothermal synthesis of In_2S_3/g-C_3N_4 heterojunctions with enhanced photocatalytic activity. *J. Colloid Interface Sci.* **2014**, *43*, 9–15. [CrossRef] [PubMed]
35. Chen, J.; Shen, S.; Guo, P.; Wu, P.; Guo, L. Spatial engineering of photo-active sites on g-C_3N_4 for efficient solar hydrogen generation. *J. Mater. Chem. A* **2014**, *2*, 4605–4612. [CrossRef]
36. Fan, M.; Hu, B.; Yan, X.; Song, C.; Chen, T.; Feng, Y.; Shi, W. Excellent visible-light-driven photocatalytic performance of Cu_2O sensitized $NaNbO_3$ heterostructures. *New J. Chem.* **2015**, *39*, 6171–6177. [CrossRef]
37. Nayak, S.; Mohapatra, L.; Parida, K. Visible light-driven novel g-C_3N_4/NiFe-LDH composite photocatalyst with enhanced photocatalytic activity towards water oxidation and reduction reaction. *J. Mater. Chem. A* **2015**, *3*, 18622–18635. [CrossRef]
38. Jin, X.; Fan, X.; Tian, J.; Cheng, R.; Li, M.; Zhang, L. MoS_2 quantum dot decorated g-C_3N_4 composite photocatalyst with enhanced hydrogen evolution performance. *RSC Adv.* **2016**, *6*, 52611–52619. [CrossRef]
39. Scofield, J.H. Hartree-Slater subshell photoionization cross-sections at 1254 and 1487 eV. *J. Electron. Spectrosc. Relat. Phenom.* **1976**, *8*, 129–137. [CrossRef]